Effect of cable surface characteristics and flow turbulence on the aerodynamic behaviour of stay cables in dry conditions

Sean McTavish [*], Annick D'Auteuil, Arash Raeesi

National Research Council Canada, Ottawa, Canada

ARTICLE INFO

ABSTRACT

This article describes a wind-tunnel study to evaluate the aerodynamic behaviour of stay cables of a bridge with various surface geometries in dry conditions. Nine cable models were fabricated and tested. Aerodynamic forces acting on the static models were measured for different wind speeds, cable-wind angles and cable axial rotation angles, in smooth and turbulent flow. The aerodynamic forces of bare, round cable models with different roughness levels were used as a baseline to compare the aerodynamic loading of the cables with surface geometry features. A comprehensive database of existing and emerging cable geometries in a wide range of flow conditions and cable-wind angles was generated. The trends exhibited by models with geometric features are similar to results available in the open literature. The aerodynamic drag coefficient was largely affected by the presence of cable surface geometry. The model with helical strakes had the lowest drag coefficient throughout the range of Reynolds numbers that was evaluated. It was observed that turbulence had a similar effect on all models, resulting in a reduction of the drag coefficient at lower Reynolds numbers and an earlier increase in drag that is associated with the supercritical Reynolds number regime. The presence of turbulent flow resulted in higher drag coefficients at high Reynolds numbers. An important secondary finding was that models fabricated with the Selective Laser Sintering (SLS) technique have a higher surface roughness than high-density polyethylene (HDPE) stay cable sleeves but when printed, they have a similar surface roughness.

1. Introduction

Cable-stayed bridges have been used in increasingly diverse situations over the past three decades. Stay cables are made with a bundle of steel cables that are fed through a high density polyethylene (HDPE) tube. The use of HDPE tubes has some drawbacks in regards to the aerodynamic characteristics of stay cables. The smooth surface of the tube can lead to rain-wind-induced vibrations. The potential sensitivity of stay cables to wind-induced vibrations can be reduced by increasing the structural damping of the stays, by altering the surface of the HDPE tube with a geometric treatment such as a helical fillet or a pattern-indented surface, or by installing cross-ties between the stays (Kumarasena et al., 2007). In addition, the aerodynamic drag coefficient of the stay cable array at high Reynolds number in dry conditions is an important parameter for the required design wind loads. Stay cable designs developed to prevent rain-wind-induced vibration or ice accretion should have a low drag coefficient (C_D) and provide stability in dry conditions.

The terminology of Zdravkovich (1997) is used in this article to describe the different flow regimes that can be present on an inclined cable. For a smooth circular cylinder, Zdravkovich described several distinct regimes that characterize the transition in the boundary layer (TrBL). In the TrBL regimes, the transition from laminar to turbulent flow for a smooth circular cylinder will occur in the boundary layer or in a separation bubble. The lift and drag coefficients experience large variations between a Reynolds (Re) number of 10^5 and 10^6. Many engineering structures, including stay cables, operate in the range of Reynolds numbers that correspond to the TrBL regimes.

The TrBL1 and TrBL2 regimes occur in the critical Reynolds number regime and the TrBL3 occurs at Reynolds numbers that are assumed to be in the supercritical Reynolds number regime. The drop in drag associated with the onset of the TrBL1 and TrBL2 regimes can occur at lower Reynolds numbers than those listed above, due to surface roughness effects, turbulent flow, eccentricities in cable shape, and for inclined cables (D'Auteuil, 2010). Dry galloping of an inclined stay cable has been linked to the drop in drag and fluctuations in lift associated with the TrBL1 and TrBL2 regimes in the critical Reynolds number range near a Reynolds number of 270,000 (McTavish et al., 2018). The critical Reynolds

number regime and the associated drop in drag can occur much earlier for inclined stay cables with ice accretion (Demartino et al., 2015).

Most existing cable-stayed bridges either have stay cables with a helical fillet or a pattern-indented surface in order to prevent the onset of rain-wind induced vibration (RWIV). Kleissl and Georgakis (2012b) compared these commonly-used surface geometries to a bare high-density polyethylene (HDPE) model to generate a database of lift and drag coefficients. Wind tunnel experiments were conducted in cross-flow and with inclined cables, where the cable-wind angle was varied from 40° to 75°. Mean and unsteady forces are presented, along with near-wake and surface-flow visualization (Kleissl and Georgakis, 2012b). It was found that transition occurred at lower Reynolds numbers for decreasing cable-wind angles for the helical fillet, whereas the critical Reynolds number range was insensitive to changes in the cable-wind angle for the pattern-indented surface. Pattern-indented surfaces have been tested by several authors and have been demonstrated to disturb the formation of a rivulet while promoting early boundary layer transition and maintaining a near-constant drag coefficient (Miyata et al., 1998; Hojo et al., 2000; Kleissl and Georgakis, 2012b; Hojo, 2015; Katsuchi et al., 2017).

A comparison of the force coefficients of several novel cable surface geometries has been presented in a series of papers from the Technical University of Denmark and the University of Aarhus (Kleissl and Georgakis, 2012a; Burlina et al., 2016b, a). The novel geometries included cylindrical vortex generators, an indented helix pattern, staggered helical strakes, circumferential strakes, and a new concave cross-sectional shape for a helical fillet or strake. In addition to these new concepts, those studies also evaluated cables with a pattern-indented surface, a traditional helical fillet, and spiral protuberances (numerous, wide fillets per pitch). The results demonstrated that the pattern-indented surface has early boundary layer transition and a near-constant C_D of approximately 0.6–0.65 in the supercritical Reynolds number regime (Kleissl and Georgakis, 2012a). The authors observed that a concave helical fillet had a higher C_D than a typical rectangular helical fillet due to its taller profile (Burlina et al., 2016a). In cross-flow, the staggered helical strake geometry was identified as a promising surface geometry. The shape provided a gradual drop in C_D throughout the critical Reynolds number regime, a drag coefficient of approximately 0.65 at high speeds, and a mean lift coefficient near zero.

In addition to a cable's surface geometry, the other parameters which have a significant impact on lift and drag coefficients are the turbulence in the flow, the cable's cross-sectional circularity and the surface roughness. Matteoni and Georgakis (2012) measured the surface roughness and circularity of a smooth HDPE cable model and characterized the effect of angle of attack and turbulence intensity on the lift and drag coefficients. Matteoni and Georgakis (2012) observed that an increase in turbulence intensity from 0.5% to 1% resulted in an earlier transition in the boundary layer and an associated earlier drop in C_D. Additionally, it was observed that the peaks in mean C_L were reduced with the increased level of turbulence.

The surface roughness of HDPE stay cable models has been characterized recently by Matteoni and Georgakis (2012) and Benidir et al. (2015). The mean roughness of HDPE sections is generally on the order of 1–2 μm based on results reported in literature. A study by Hojo et al. (2000) systematically varied the mean roughness of stay cable models with evenly-distributed roughness elements that changed the mean roughness of models from 3 μm to 1500 μm. Although the results for the roughened cable models in Hojo et al. (2000) are limited to the sub-critical and critical Reynolds number regimes, it was demonstrated that the critical Reynolds number becomes lower as the roughness level is increased.

Recent work at the National Research Council Canada (NRC) has quantified the effect of the cross-sectional eccentricity of a stay cable on its response. A comprehensive study by Christiansen et al. (2017) identified the sensitivity of lift and drag forces to eccentricity of the cable shape using scaled models that were based on detailed geometric scans of

actual bridge cables. Additionally, Yamauchi et al. (2016) provided further supporting evidence that the vibration response of a full-scale cable model can be influenced by the axial rotation of the cable, and therefore its cross-sectional eccentricity. A typical shape deviation for a full-scale stay cable is on the order of 1% of the cable diameter (Matteoni and Georgakis, 2012; Larose and D'Auteuil, 2014; Benidir et al., 2015). As a result, it has become recommended practice at the NRC to scan and characterize the shape of HDPE stay cable models (McTavish et al., 2018; D'Auteuil et al., 2019). The current study controls the cable shape in a way that allows the cable surface geometry and surface roughness to be evaluated independently.

The objectives of the study were to evaluate the aerodynamic forces for static stay cable models with different cable surface geometries (helical fillet, rings, helical strakes, pattern-indented surface), in smooth and turbulent flow, and to complement existing data in the open literature. These new cable surface treatments need to be evaluated under dry conditions to measure the impact on the drag force and on the overall aerodynamic behaviour of a stay cable.

The current manuscript provides a detailed wind-tunnel investigation of the drag and lift coefficients of stay cables with various surface geometry features. Data from nine cable models were evaluated and the aerodynamic forces (along-wind and across-wind) were measured as a function of wind speed (U), inclination angle (θ), yaw angle (β), and axial rotation (α). The article describes the experimental setup, the cable models and, the drag and lift coefficient results for the cable models.

2. Cable models and fabrication

Eight models were tested in the current study. Seven of these cable models were fabricated using the Selective Laser Sintering (SLS) rapid prototyping technique to print the desired cable shape and, the eighth cable was made in polyethylene. SLS sleeves were fabricated in sections of 300 mm and were then glued together to form the total cable model length of 1500 mm. The outer diameter of the physical cable models was 88.9 mm (3.5 in) and represents a scaling factor of 2.25 compared to a typical full-scale stay cable with a diameter of 200 mm. The scaling factor was required to minimize the blockage of the flow in the test section and maximise the cable length-to-diameter ratio (larger than 15) while still being able to measure the drag and lift forces for a range of Reynolds numbers that are representative of the flow conditions experienced by a full-scale stay cable. Nominally, the precision of the SLS printer operated by NRC has been estimated to be 0.25 mm in the longitudinal and transverse directions.

The models numbered 1 to 7 all had a circular cross-section. Model 8 was based on a scan of an in-service stay cable and had eccentricities in its cross-sectional shape. In addition to the 8 models that were tested in the wind tunnel, data acquired in 2017 with the same setup for a model with a helical fillet will be used in this paper (Model 9). Cable models with a bare surface and with four surface geometries (double helical fillets, concentric rings, a pattern-indented surface, and double helical strakes) were evaluated in this study. These cable surface geometries were selected as they represent typical geometries used on existing stay cables of bridges or emerging geometries for which published data are available in literature (Kleissl and Georgakis, 2012a). All of the cable models included in the current study are summarized in Table 1, are shown in Fig. 1, and are described in more detail below.

2.1. Bare cable models

Three bare (B) cables with a circular cross-section were evaluated to characterize the effect of surface roughness on aerodynamic force coefficients. The terminology "bare" is equivalent to a geometrically-"smooth" cable surface, but is used in the current article to avoid confusion when using terms such as "smooth" flow and to avoid referring to "smooth" models that have different levels of surface roughness. The bare cable terminology used in this study means "no added surface

Table 1
Summary of the cable model geometry. All dimensions are provided at model scale.

Surface Geometry	Model Name	Texture	Geometry Dimensions
Bare	1-Bare/SLS	SLS	–
Bare	6-Bare/Paint	SLS + Paint	–
Bare	5-Bare/PE	PE	–
Helical Fillet	8-JRSS13b-HF/Paint	SLS + Paint	1.75% × 0.88%D πD pitch, helix angle 45°
Helical Fillet	9-Fillet/SLS	SLS	1.04%D × 3.12%D πD pitch, helix angle 45° D = 96.15 mm
Helical Strakes	3-Strakes/SLS	SLS	1.04%D × 3.12%D 44.67 mm arc length 161.25 mm pitch, helix angle 60°
Pattern-indented (Dimples)	4-Dimples/SLS	SLS	full-scale pattern details in Katsuchi et al. (2017)
Rings	2-Rings/SLS	SLS	1.04%D × 3.12%D (width × height) 1D centre-to-centre
Rings	7-Rings/Paint	SLS + Paint	1.04%D × 3.12%D 1D centre-to-centre

geometry".

1-Bare/SLS This round model was fabricated from SLS and represents the as-printed surface finish from the 3D printing process.

6-Bare/Paint This round model was fabricated and tested originally in 2015 by Christiansen et al. (2017) and was tested in a wider range of conditions in the current study. The cable is fabricated from SLS, but has been sanded and painted to provide a surface finish similar to an HDPE tube. Because of its repeated use, the model had some surface scratches and glue residue from a previous test in 2015.

5-Bare/PE Model 5 was fabricated out of polyethylene (PE) to represent the average roughness characteristics of an extruded HDPE sleeve of a stay cable. The inner diameter was bored to match the inner diameter of the SLS models and the outer diameter was machined on a lathe to a diameter of 88.9 mm. This step was necessary because off-the-shelf tubes and typical HDPE sleeves of stay cables do not have a nominally circular cross-section. Machining the outer surface allowed for a controlled comparison of surface roughness effects between SLS and PE models of the same cross-sectional geometry. The machined outer surface has a uniform surface finish, whereas an HDPE stay cable will have a non-homogeneous surface finish that may consist of spanwise striations, surface imperfections, or labelling that will cause localized variations in surface roughness.

2.2. Models with surface geometry features

8-JRSS13b-HF/Paint The US Federal Highway Administration (FHWA) carried out measurements of the cross-sectional shapes of in-service stay cables on three in-service bridges in the USA in 2015 using a custom-built scanning robot (Bosch and Pagenkopf, 2017). The model was originally referred to as JRSS13b-HF and had previously only been tested at a yaw angle of 0° and in smooth flow. Therefore, to increase the database of aerodynamic force coefficients, the same model was tested over a range of yaw angles in smooth and turbulent flow in the current study.

9-Fillet/SLS Model 9 was fabricated for a wind tunnel test that took place in 2017 and was not tested again in the current measurement campaign but the data are presented in this paper for comparison purpose. The cable had an as-printed SLS surface finish and, unlike the models in the current study, an outer diameter of 96.15 mm. The surface geometry cross-section on this model is consistent as a percentage of model diameter with the models with rings (Models 2 & 7), and with the model with helical strakes.

3-Strakes/SLS The helical strake geometry in the current study has been developed using parameters available in literature (helix angle, strake height) and parameters estimated from images (strake length, strake spacing). Unlike the concave cross-sectional geometry used by Kleissl and Georgakis (2012a), a rectangular strake cross-section was used in the current study. This was done to provide a consistent cross-sectional shape between cable models with a helical fillet (Model 9), with rings (Models 2, 7), and the model with helical strakes (Model 3).

4-Dimples/SLS The surface geometry, also called pattern indented, that was selected was based on the pattern used for the Tatara Bridge and described in Katsuchi et al. (2017). The full-scale indentation dimensions (for a stay cable diameter of 140 mm) were scaled down for the model
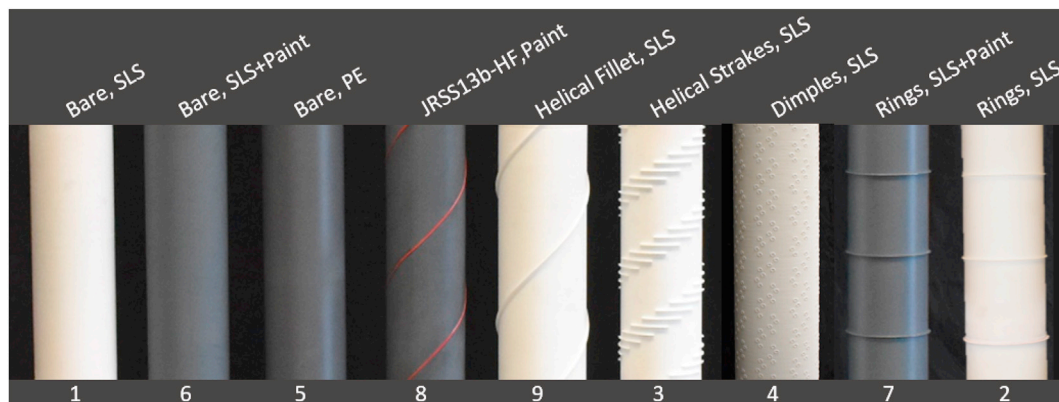
Fig. 1. Closeup view of dry cable models.

diameter of 88.9 mm. The width of the ridge around the indentation was estimated using images from Kleissl and Georgakis (2012b) and was approximated as a ring with a semicircular cross-section around the elliptical indentation.

2-Rings/SLS Stay cable models with circumferential strakes, or concentric rings, have been evaluated by Kleissl and Georgakis (2012a) as a potential RWIV mitigation measure. A concentric ring design has been implemented on the Champlain Bridge in Montréal. As a result, this stay cable geometry represents a new technology that needs to be fully-understood in the context of dry conditions. Two variations of the same physical model were evaluated during the current study. The concentric ring design in the current study had a rectangular cross-sectional shape that was consistent with the helical fillet (Model 9) and helical strake (Model 3) cross-sections. Model 2 had an as-printed SLS texture.

7-Rings/Paint In the middle of the test campaign, it was decided to sand and paint Model 2. The new, smoother, model was renamed as Model 7 and was used to establish the sensitivity of the aerodynamic behaviour of the ring geometry to the roughness of the base cable material.

3. Model surface roughness

The importance of quantifying and reporting the cable surface roughness in an experiment has been recognized recently by the cable research community, and several factors, including boundary layer transition, flow separation, and cable forces can be affected by roughness. The surface roughness of the models used in the current study was measured using a handheld Mitutoyo Surftest SJ-410 roughness tester. The roughness tester traces a stylus along the surface of an object over a prescribed distance and measures several roughness characteristics. The mean roughness parameter (R_a) is commonly used to characterize the surface roughness of stay cables. This parameter characterizes the mean vertical deviation measured over a certain distance or number of points. Each roughness measurement was taken over a distance of 4.8 mm in the cable's axial direction, following the surface roughness measurement settings of the Standard ISO 1997. Roughness measurements were recorded on the three bare cable models (Models 1, 5, 6) and on the painted model with rings (Model 7). Measurements were taken at cable axis rotation angles of $0°$, $90°$, $180°$, and $270°$. For Models 5,6,7, measurements were acquired 300 mm from the bottom, at the middle, and 300 mm from the top of the cable at each axis rotation angle, for a total of 12 measurements per cable. The bare cable with an as-printed SLS

finish (Model 1) had a surface roughness that had greater variation along its span and, as a result, measurements were acquired in the centre of each segment of the SLS model and near the sanded, smoothed joints, for a total of 28 measurements.

Few surface roughness measurements have been made on HDPE sheathing of in-service bridges. HDPE sections used for long-term monitoring have been installed near the cable stays on the Øresund bridge in Denmark and measurements of these sections have been published in literature (Larose et al., 2003; Matteoni and Georgakis, 2012). Roughness data for the Øresund bridge described by Matteoni and Georgakis (2012) include measurements on HDPE sections with little mechanical degradation and on HDPE sections with increased surface degradation. Field measurements were made during the current study to characterize the roughness of the HDPE sheathing on the pedestrian bridge over the Airport Parkway in Ottawa, Canada (Fig. 2). The measurements were made approximately 2 m above the deck height on the third cable (counting from the east end of the bridge) on the north and south sides of the bridge. The stays that were measured are identified in Fig. 2. The HDPE was heavily scratched near the deck level but a uniform, unscratched section of the stays was measured with the roughness tester. Two measurements on each stay cable resulted in an average R_a of 2.47 μm. These stay cables have a diameter of approximately 90 mm and therefore have an average non-dimensional roughness value ($\varepsilon = R_a/D$) of 27.5×10^{-6}.

The roughness values from field measurements, from experiments in literature, and from previous work at NRC have been tabulated in Table 2. In general, many stay cables and models have a mean roughness value on the order of 1–2 μm. The normalized roughness parameter, ε, varies from approximately 3×10^{-6} to 27×10^{-6} for in-service stay cables or for experiments that used actual HDPE sections. The mean roughness values from the four cables measured in the current study are compared in Table 2. Good control over the sanding and painting process has been established and this resulted in the PE and painted SLS models having similar levels of roughness. The as-printed SLS surface texture has a roughness that is on the order of 6 times greater than the PE and painted models. The sanded and painted SLS cable models at NRC have an absolute R_a that is similar to in-service stays, but a normalized roughness value that is near the upper end of the range of ε observed for in-service stay cables, due to the use of a scaled diameter. The aerodynamic behaviour of the sanded and painted models are compared in this paper to the model made from PE (which is similar to HDPE) to determine how representative the SLS models are of real stay cables.

(a) View of the Airport Parkway bridge.   (b) Cable 3-North, looking north.

Fig. 2. Field measurements on the Airport Parkway bridge in Ottawa, Canada.

Table 2
Comparison of surface roughness measurements at NRC with available data from literature.

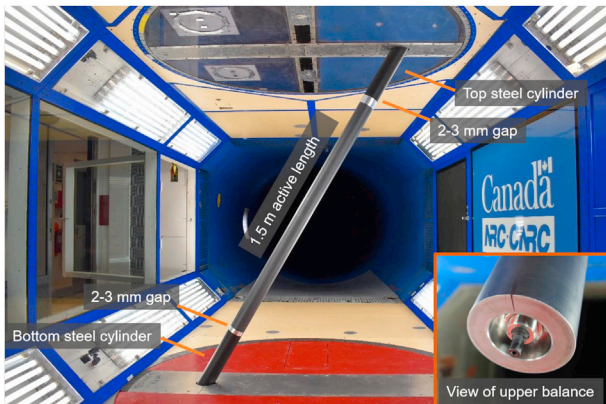| Cable	Surface	R_a [μm]	D [mm]	$\varepsilon = R_a/D$ $\times 10^{-6}$	Reference
Øresund bridge	HDPE	–	250 mm	3.9	Larose et al. (2003)
	HDPE	–	160 mm	6.5	
DTU - Øresund	HDPE - smooth	0.7 to 1	250 mm	2.8 to 4	Matteoni and Georgakis (2012)
DTU - Øresund	HDPE - degraded	4 to 5	250 mm	16 to 20	
NRC - Ottawa, Airport Parkway	HDPE	2.47	90 mm	27.5	Current Study
DTU - Static	HDPE	0.7 to 2.05	160 mm	4.38 to 12.8	Matteoni and Georgakis (2012)
CSTB	HDPE	1.29 to 1.43	250 mm	5.16 to 5.72	Benidir et al. (2018)
NRC - Static	Painted SLS	1.56	88.9 mm	17.5	Christiansen et al. (2017)
NRC - Dry Galloping, Dynamic	HDPE	0.836 to 1.143	217 mm	3.82 to 5.22	McTavish et al. (2018)
NRC - RWIV	HDPE	Mean = 1.964 StDev = 0.742	218 mm	9.01	D'Auteuil et al. (2019)
NRC - 1-*Bare/SLS*	Bare, SLS	Mean = 9.46 StDev = 1.75	88.9 mm	106	Current Study
NRC - 5-*Bare/PE*	Bare, PE	Mean = 1.56 StDev = 0.08	88.9 mm	17.5	
NRC - 6-*Bare/Paint*	Bare, SLS + Paint	Mean = 1.31 StDev = 0.19	88.9 mm	14.7	
NRC - 7-*Rings/Paint*	SLS + Paint	Mean = 1.07 StDev = 0.27	88.9 mm	12.1	

4. Experimental setup

4.1. NRC 2 m × 3 m wind tunnel

The aerodynamic study of dry-stay-cable models was performed in the NRC 2 m × 3 m Wind Tunnel in Ottawa, Canada. The wind tunnel is a closed circuit atmospheric facility with a test section of 2.7 m wide by 1.9 m high and 5.2 m long. The maximum wind speed is around 130 m/s allowing tests to match the Reynolds number of prototype stay cables. The size of the test section makes the tunnel ideal for scaled models of stay cables and accommodates models with length-to-diameter ratios (aspect ratio) higher than 15. The tunnel is equipped with floor and roof turntables capable of changing the model orientation with respect to the main wind flow.

4.2. Model installation

The setup of the model in the wind tunnel, including an inset view of the upper balance connection, is shown in Fig. 3. The models consisted of an SLS or PE stay cable slid and then clamped onto a carbon fibre tube with an outer diameter of 73.2 mm. The live section of the model on which forces are measured was 1500 mm in length, corresponding to a length-to-diameter ratio of 16.9. The assembled model is clamped to balances located inside the top and bottom dummy fairings. These dummy fairings are anchored outside of the shell of the test section but no forces are measured on these parts. It is assumed that the use of

dummy fairings provides representative end conditions for the live section of the model. A narrow gap was maintained between the live section of the cable model and the dummy fairings to avoid mechanical fouling. The wind tunnel tests were conducted for a cable inclination angle of 60° from the horizontal, as shown in Fig. 3, since a cable inclination of 60° is the minimum inclination that can be used to attach the top and bottom of the model directly on the floor and ceiling turntables. An inclination of 60° represents also many cases for stay cables of in-service bridges.

4.3. Experimental conditions

The blockage area ratio, evaluated as the ratio of the model diameter and the wind tunnel width, was 3.6%. The results of the tests were not corrected for blockage since it was believed that the uncertainties associated with the corrections for such cases would be similar to the magnitude of the corrections themselves. The drag coefficient uncorrected for blockage provides conservative values.

Tests were carried out in smooth flow and in turbulent flow. In smooth flow, the turbulence intensity in the along-wind direction was $I_u < 0.14$ % and the uniformity of the mean wind speed at the position of the model was well within 0.5% of the mean wind speed in the test section. Cable-stayed bridges are exposed to turbulent flow with vortices created by the surrounding environment. As an attempt to evaluate the

Fig. 3. View of a cable model mounted at θ = 60°, β = −90°.
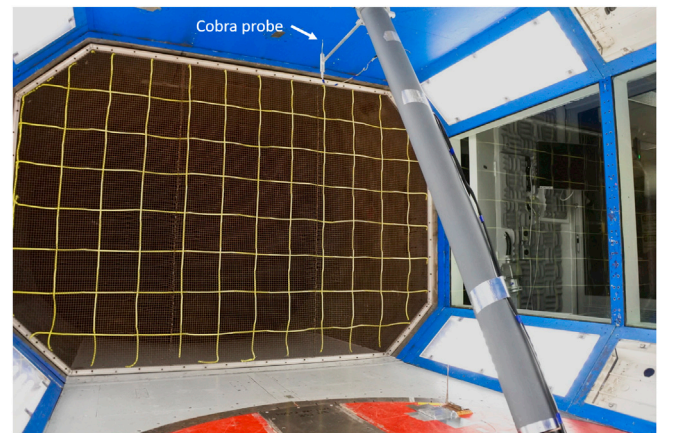
Fig. 4. Turbulence system for cable testing: Inlet grid with 23 cm × 23 cm mesh size. The Cobra probe used to measure the flow properties was supported upstream of the model.

Fig. 5. Turbulence system for cable testing: Two flat wood plates are used in the settling chamber to generate low frequency turbulence.

impact of wind turbulence on the aerodynamic behaviour of models of the stay cables, a grid upstream of the test section and large obstacles installed in the settling chamber were used to increase the level of turbulence at the model location. This turbulence system was used to develop a generalized understanding of the effect of turbulence on the forces on cable models. The main grid frame was mounted 1.92 m upstream of the middle of the turntable of the test section. The main grid frame was composed of fine bar sizes of 1.55 mm in diameter with a square mesh size of 10.67 mm and is combined with yellow polypropylene twisted ropes of 7 mm diameter inserted through the main frame mesh to obtain a larger mesh of 0.23 m × 0.23 m (see Fig. 4). Two large, flat wooden plates (0.6 m wide × 2.4 m high, separated by 0.9 m) were also installed in the settling chamber of the NRC 2 m × 3 m Wind Tunnel (see Fig. 5). Stay cables of a bridge are exposed to small vortices as well as large vortices created by the surrounding landscape that will change the flow direction and impact the cable boundary layer. The

simulation of turbulence using a grid and large obstacles was intended to capture both smaller vortices (high frequency) and medium vortices (lower frequency) that have an impact on the boundary layer transition.

The characteristics of the flow turbulence were measured using a Cobra probe from Turbulent Flow Instrumentation that can measure the three components of the wind. The flow survey allowed the variation in turbulence intensity to be characterized both spatially over the envelope of the model and as a function of speed. The cable was installed in the test section during these measurements and a support arm held the fast-response pressure probe 4.7D upstream of the cable. Measurements were conducted in a streamwise-vertical plane when the cable was at a yaw angle of 0°(using the experimental setup shown in Fig. 4), and in a lateral-vertical plane when the model was at a yaw angle of 90°. The results of the flow survey are shown in Fig. 6a and b, including a schematic of the cable orientation and wind direction in each plot. Fig. 6a shows the turbulence intensity values calculated at several heights above the ground along the tunnel vertical-streamwise plane. The turbulence intensity values at the three points labelled as A, B, C are plotted as a function of speed over the range of speeds that were covered during the flow survey. It can be seen that above 10 m/s, the turbulence intensity is fairly constant as a function of speed at each point in space. There is a spatial variation in turbulence over the height of the model, where the turbulence intensity tends to decrease further away from the floor of the tunnel. Fig. 6b shows the results of the flow measurements that were obtained at several locations in the lateral-vertical plane. The turbulence intensity results in Fig. 6b show only a minor dependence on wind speed. There is a variation in the spatial distribution of the turbulence intensity, and the data point located near the upper-right corner of the model (when looking downstream) has the lowest magnitude. The turbulence-generation system resulted in a longitudinal turbulence intensity I_u that varied in space between 3.3% and 5.6%, but that did not vary significantly with wind speed. The longitudinal integral length scales were approximately 0.1 m; on the order of the model diameter. As mentioned previously, the turbulence generating system was used to develop a generalized understanding of the effects of a turbulent flow environment on cable forces, and the turbulence characteristics do not represent a specific set of conditions that would be encountered on a bridge.
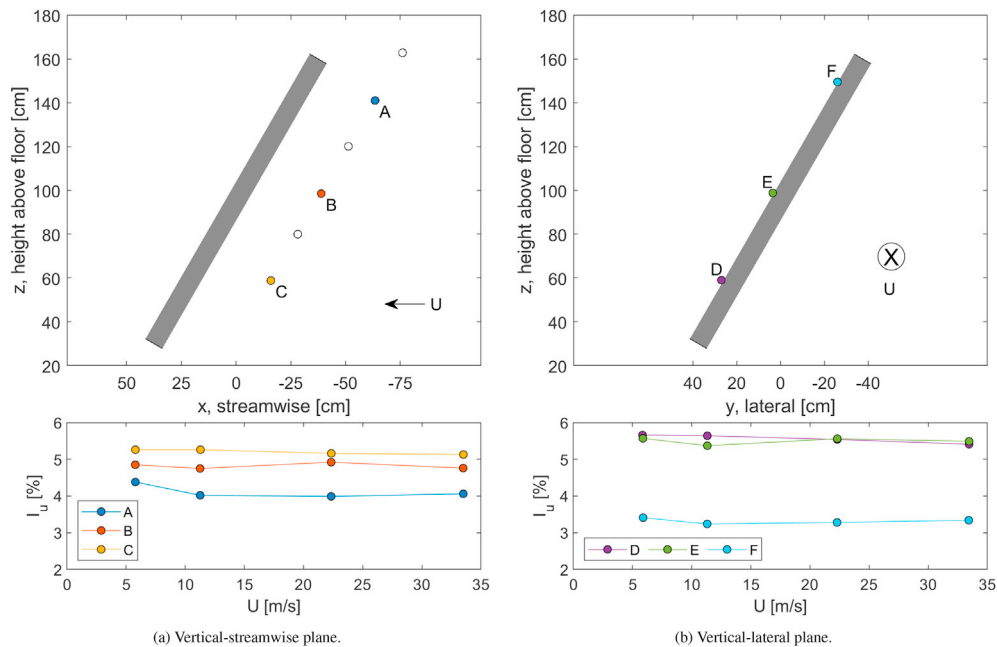

(a) Vertical-streamwise plane.

(b) Vertical-lateral plane.

Fig. 6. Turbulence intensity results as a function of speed at several locations in the test section of the wind tunnel. The Cobra probe support arm was mounted to the cable and the probe tip was located 4.7D upstream of the model.

4.4. Instrumentation and data acquisition

The model of the stay cable was instrumented with internal balances (two-axis force sensors, Honigmann RFS 150XY with a range of 600 N) to measure the along-wind and across-wind forces perpendicular to the model axis (Fig. 3, inset). The balances were inserted at both extremities of the dummy sections and the central part of the model of the stay cable was clamped on the bearing journals of the force sensors which were protruding from the dummy sections. The two balances were carefully aligned to ensure that the along-wind sensors were installed fully parallel to the flow direction at a 0° yaw angle. The sensors were calibrated in-situ using calibrated weights. All analog outputs from the load sensors were passed through an anti-aliasing filter (a low-pass filter at 485 Hz) prior to being sampled simultaneously at a frequency of 1250 Hz for a period of 60 s. The flow characteristics were measured by the data acquisition system of the NRC 2 m × 3 m Wind Tunnel, including the measurement of the total pressure, static pressure, barometric pressure and air temperature. These flow measurements were used to define the mean dynamic pressure, wind speed, air density and air viscosity for each test point.

5. Data reduction

5.1. Force coefficients

Aerodynamic force coefficients were calculated at the completion of each test run. Fig. 7 illustrates a schematic of the cable-wind relative orientation where θ, β, and φ are respectively the inclination, yaw, and cable-wind relative angle. A yaw angle of 0° is defined as aligned with the cable main axis and with wind flow moving downward along the cable main axis. A negative yaw angle corresponds to a counterclockwise rotation of the turntable when viewed from above. The freestream wind speed (U) has a component that is normal to the cable axis, but still aligned in the cable-wind plane ($U_N = U\sin\varphi$). The plane formed by the

angle between the cable-wind plane and the vertical cable plane (α_N) is parallel to the cable cross-section and is aligned with U_N.

The cable-wind angle (φ) and the angle between the vertical cable plane and the wind component normal to the cable axis (α_N) are calculated using Equations (1) and (2). The relationship in Equation (2) is derived in Cheng et al. (2008).

$$cos\ \varphi = \cos\beta\cos\theta \tag{1}$$

$$tan\ \alpha_N = \frac{tan\ \beta}{sin\ \theta} \tag{2}$$

The forces acquired at the top ($F_{X2}F_{Y2}$) and bottom ($F_{X1}F_{Y1}$) of the cable are transformed such that the forces are aligned in the along-wind and across-wind directions normal to the cable axis.

The drag and lift coefficients were based on the summation of the two load cells in the along-wind and across-wind directions normal to the cable axis, respectively:

$$C_D = \frac{\left(D_{top} + D_{bot}\right)}{0.5\rho U^2 DL} \tag{3}$$

$$C_L = \frac{\left(L_{top} + L_{bot}\right)}{0.5\rho U^2 DL} \tag{4}$$

In Equations (3) and (4), C_D is in the along-wind direction and C_L is in the across-wind direction, U is the incoming flow speed, ρ is the air density, D is the model diameter and L is the length of the live part of the cable model. The line of action of the drag and lift forces in the along-wind and across-wind directions normal to the cable axis, respectively, are shown in Fig. 7. Drag and lift in this article therefore refer to the components normal to the cable axis, aligned with U_N. The Reynolds numbers are calculated using the base stay cable diameter D for each model and the incoming flow speed U.

6. Test program

The wind tunnel tests were carried out for a cable inclination (θ) of 60° with respect to the horizontal. In general, stay cables of a bridge can be inclined between approximately 25° to 70°. A cable inclination of 60° allowed the cable model to be mounted within the turntables at the floor and ceiling of the NRC 2 m × 3 m Wind Tunnel and to use the motion system for yaw rotation. A common range of 7 yaw angles was selected for each cable: 0°, −30°, −60°, −90°, −120°, −135°, −150°. These yaw angles correspond to cable-wind angles of 60°–115°. A speed sweep was conducted between 4 and 80 m/s in smooth flow and between 4 and 58 m/s in turbulent flow for each yaw angle. In addition, for certain runs the cable was rotated about its main axis to evaluate model-eccentricity effects. In total, more than 180 speed sweep tests were carried out for different combinations of models, yaw angles, flow types, and cable rotation angles. Model 2 was only tested in smooth flow, but all other models were tested in both smooth and turbulent flow.

7. Results

The mean drag and lift coefficient results are presented in this section. Each cable model has been assigned a unique color and each yaw angle has been assigned a unique marker shape. Smooth flow results are connected with a solid line with white color-filled markers, whereas turbulent flow data points are connected with a dashed line and the markers are colour-filled.

7.1. Repeatability

The repeatability of the experimental setup was assessed using two different models in smooth and turbulent flow. The force coefficients in Fig. 8 demonstrate very good repeatability with same behaviour of the
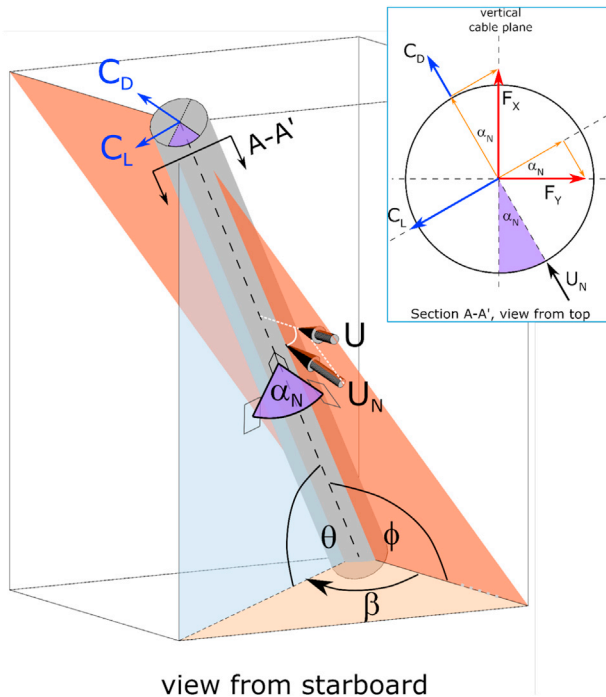

Fig. 7. Definition of the cable-wind plane, the wind speed normal to the axis of the cable, and the along-wind and across-wind directions normal to the cable axis. A positive yaw angle is shown. The inset shows the transformation of forces from balance axes to along-wind and across-wind directions normal to the cable axis.
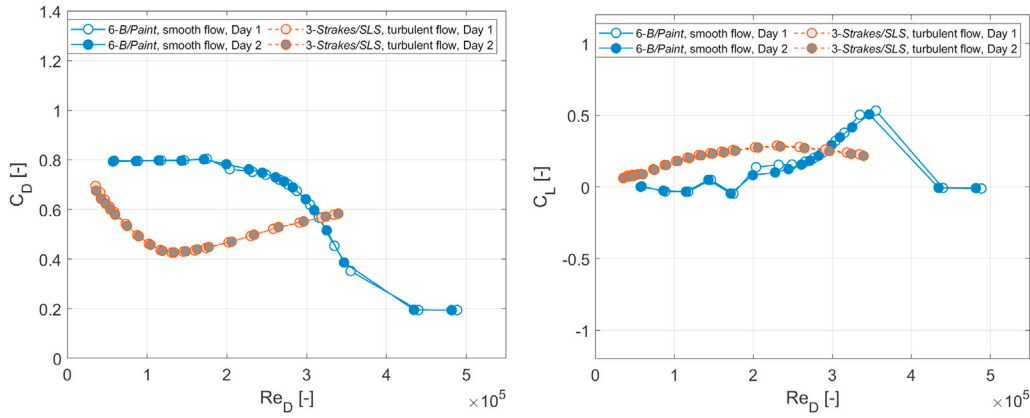
Fig. 8. Repeatability of force coefficients for two models, $\varphi = 60°$. Model 6-*Bare/Paint* had an axial rotation angle of 90° in both cases shown.

drag coefficient and lift coefficient with Reynolds number for two runs. The variation in drag coefficient on the order of 2–3% is typical within the critical Reynolds number range due to the aerodynamic instability of the separation bubble, especially in smooth flow.

An overnight repeat was conducted for Model 6-*Bare/Paint* without disturbing the model, whereas the repeat for Model 3-*Strakes/SLS* was conducted on a separate day and after speed sweeps had been conducted at several other yaw angles. It should be noted that the internal balances used to measure the forces on the cable model had a full range of 600 N to prevent overload at high speed for cables with a drag force coefficient on the order of 1.0. However, for Reynolds numbers lower than 35,000, the magnitude of the forces measured by the internal balance was in the low range of measurement, i.e. within the accuracy of the sensor. The variation of the wind speed below 4 m/s also contributed to higher uncertainty on the results. It was decided to omit the data points acquired at a Reynolds number of 25,000 due to the increased level of uncertainty below this Reynolds number threshold. The drag force for Reynolds numbers higher than 35,000 was at least twice the value of the uncertainty of the balance. A Reynolds number of 35,000 corresponds to a wind speed of approximately 2.7 m/s for a cable with a full-scale diameter of 0.2 m.

7.2. Model eccentricity

All but one of the models used in the study were fabricated to have a nominally circular cross section. The force coefficients for each model were measured at various axial rotation angles to assess the level of eccentricity of the models. The results for the four models shown in Fig. 9 indicate that the drag coefficient is essentially insensitive to changes in axial rotation α. This suggests that the models have a cross-sectional

Fig. 10. Surface characteristics of Model 6-*Bare/Paint*.

shape that is aerodynamically circular. The diameter of Model 6-*Bare/ Paint* was measured at several circumferential locations and it was established that the eccentricity of the model was between 0.2% and 0.3% of the model diameter. This level of eccentricity was consistent with the precision of the SLS fabrication process identified earlier in the manuscript. Previous works by Christiansen et al. (2017) and McTavish et al. (2018) have demonstrated that eccentricities in the shape of a model can lead to significant differences in C_D at different angles of attack. The most significant changes in C_L due to a change in the axial rotation angle shown in Fig. 9 occurred for Model 6-*Bare/Paint*. Model 6 had been used previously in 2015 and had surface imperfections which included scratches and glue residue from a previous installation/removal of a helical fillet, as shown in Fig. 10. The effect of these imperfections on C_L changes with axial rotation angle, which could account for the behaviour observed in Fig. 9, in a similar way that Matteoni and Georgakis (2012) observed that labelling on the surface of an HDPE model had an effect on the boundary layer transition of the model at certain model angles of attack. Some variations in the lift coefficient for Model 5-*Bare/PE* are also observed near a Reynolds number of 2 $\times 10^5$ in Fig. 9. These differences at two angles of attack are attributed to spanwise variations in the asymmetry of the boundary layer separation behaviour
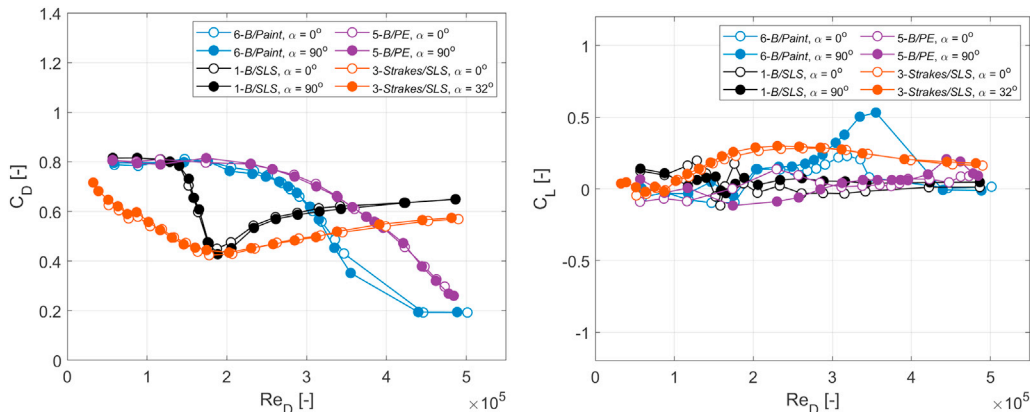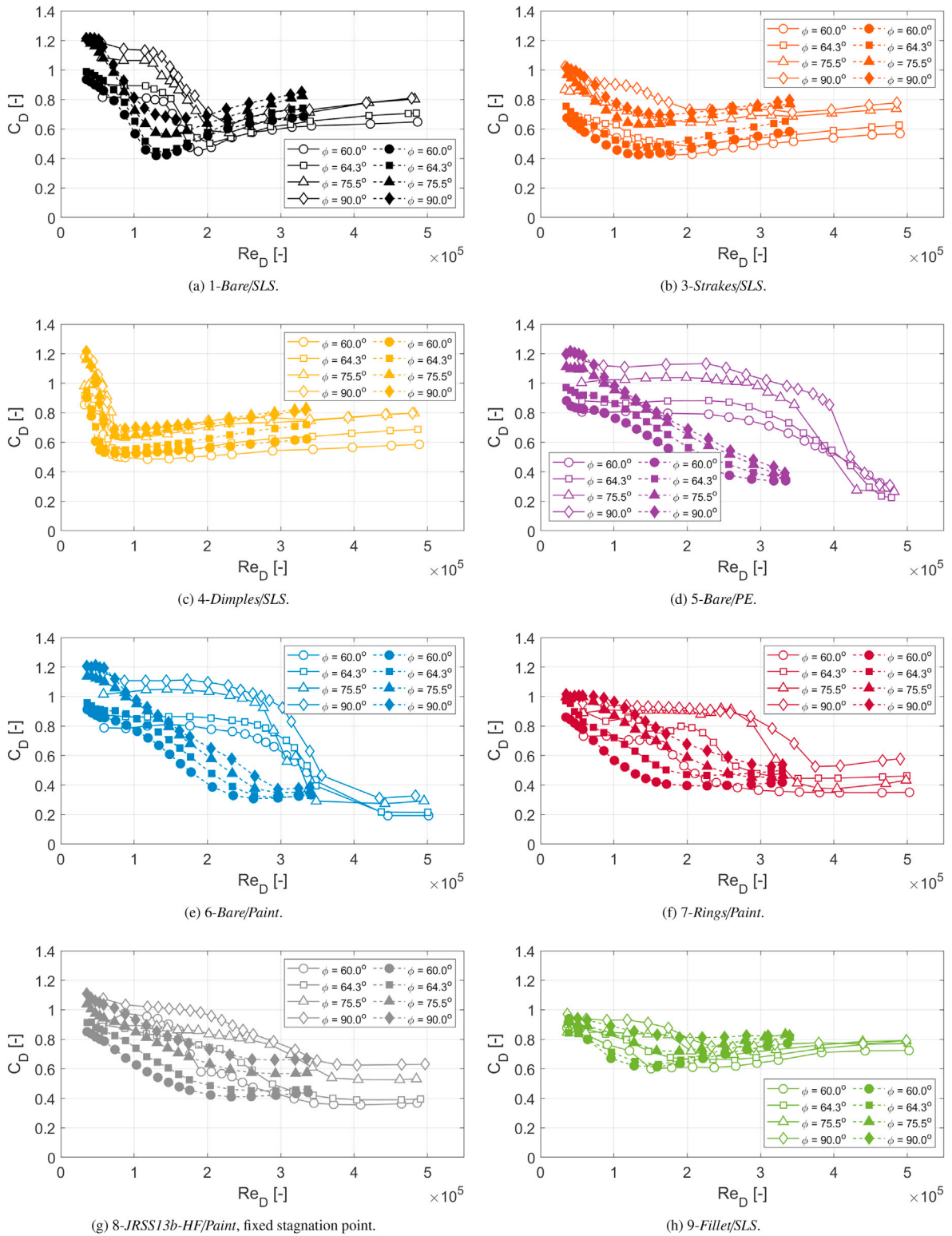

Fig. 9. Effect of axial rotation angle for four nominally round models. Smooth flow, $\varphi = 60°$.

S. McTavish et al.

(a) 1-*Bare/SLS.*

(b) 3-*Strakes/SLS.*

(c) 4-*Dimples/SLS.*

(d) 5-*Bare/PE.*

(e) 6-*Bare/Paint.*

(f) 7-*Rings/Paint.*

(g) 8-*JRSS13b-HF/Paint*, fixed stagnation point.

(h) 9-*Fillet/SLS.*

Fig. 11. Comparison of drag coefficients in smooth (white-filled markers) and turbulent flow (colour-filled markers). Note that Model 2 was not tested in turbulent flow. (For interpretation of the references to colour in this figure legend, the reader is referred to the Web version of this article.)

on both sides of the cable that may be induced by small perturbations.

7.3. Description of the model performance

The cable models were tested in smooth flow and in turbulent flow with a turbulence intensity in the range of 3.3%–5.6% and length scales

of 0.1 m over the spatial range encompassed by the cable models. The effect of turbulence is demonstrated by plotting drag coefficients for each cable model at three different φ in smooth and turbulent flow (Fig. 11). The effect of turbulence on the lift coefficient is not shown in a dedicated section, but will instead be described as part of the subsequent sections on roughness and surface geometry effects.

The force coefficients for Model 1-*Bare/SLS* in smooth and turbulent flow are shown in Fig. 11a. In smooth flow, the added model roughness (Models 5 and 6) leads to the onset of transition in the boundary layer at a Reynolds number of approximately 1.5×10^5, followed by a rise in C_D in the supercritical Reynolds number regime. The drag coefficient at the maximum Reynolds number ranges from 0.65 to 0.8 depending on the cable-wind angle. The critical Reynolds number range shifts to an even lower Reynolds number in turbulent flow (Fig. 11a).

Model 2-*Rings/SLS* was painted following tests in smooth flow, and therefore force coefficients were not available for this model in turbulent flow. The smooth-flow results for Model 2 will be shown in a later plot.

The Model 3-*Strakes/SLS* was designed based on information available in literature and had a simplified, rectangular, cross-sectional strake shape (Kleissl and Georgakis, 2012a). The cable model was already experiencing the TrBL regime at the lowest Reynolds number of this experiment. The drop in drag shown in Fig. 11b for this model over the critical Reynolds number regime is gradual, and the C_D curve exhibits two plateaus in cross-flow, before the drag coefficient increases in the supercritical Reynolds number regime. The plateaus can be observed in smooth flow for Reynolds numbers between about 0.5×10^5 to 1.1×10^5 and a second plateau between 2×10^5 and 3.5×10^5. The C_D at the maximum Reynolds number varies from 0.57 to 0.78 depending on the cable-wind angle. Similar trends (gradual drop in C_D, plateaus in C_D) are also observed for results in cross-flow in Kleissl and Georgakis (2012a). The results in Kleissl and Georgakis (2012a) with an HDPE model and the concave strake geometry present a C_D of 0.65 at a Reynolds number of approximately 325,000 and at $\varphi = 90°$. At a similar Reynolds number, the drag coefficient in Fig. 11b is 0.72. The use of a model with an SLS finish (and therefore higher surface roughness compared to HDPE) may have resulted in an upward shift in the drag behaviour in cross-flow compared to Kleissl and Georgakis (2012a). Other differences between the current results and those published by Kleissl and Georgakis (2012a) include the model aspect ratio (16.9 in the present experiment vs 9.6), the setup in the wind tunnel (dummy ends in the present experiment vs end plates), the use of blockage corrections (none in the present experiment vs Maskell-3 for cross-flow conditions in literature) and the strake cross-sectional geometry details. The impact of turbulence for the cable with helical strakes was less significant than for the Model 1-*Bare/SLS*. The reduction of the drag coefficient occurred at a similar Reynolds number range in smooth and turbulent flows for cable-wind angles of $\varphi = 60°$, $64.3°$ and $75.5°$. There is only the case at $\varphi = 90°$ for which the reduction in drag was observed at a lower Reynolds number in turbulent flow compared to smooth flow. The impact of the turbulence can be observed in the supercritical Reynolds number regime where the slope is larger in turbulent flow than in smooth flow.

The Model 4-*Dimples/SLS* is covered in a series of dimples with a raised outer edge. The behaviour of the model's drag coefficients is shown in Fig. 11c. The dimples promote an early drop in C_D, at a Reynolds number of approximately 50,000, followed by a gradual rise in C_D to a value that ranges from 0.6 to 0.8. The addition of turbulence has little effect on the initial transition behaviour of the cable with a pattern-indented surface, but results in a more rapid rise in C_D and results in values that are 0.05 higher than in smooth at a Reynolds number of 300,000. Results for a pattern-indented HDPE model from Kleissl and Georgakis (2012a) and Kleissl and Georgakis (2012b) indicate a drop in drag due to transition that occurs by a Reynolds number of 100,000 and a flat drag curve up to a Reynolds number of 300,000. At a Reynolds number of approximately 280,000, a comparison of the smooth-flow results in Fig. 11c with data from Kleissl and Georgakis (2012b) and Kleissl and Georgakis (2012a) shows a similar C_D at $\varphi = 60°$ and a C_D greater by approximately 0.1 in the current work at $\varphi = 90°$. In addition to the surface roughness of Model 4, differences between these experiments include the model aspect ratio, the application of blockage corrections, and end plates in Kleissl and Georgakis (2012b). The geometry of the dimples that were inferred from photographs could also be a

potential difference between the experiments.

The force coefficients for Models 5-*Bare/PE* and 6-*Bare/Paint* are shown in Fig. 11d and e, respectively. The smooth, uniform surface of the PE model results in drag and lift behaviour typical of a smooth cylinder in smooth flow. A drop in drag near a Reynolds number of 400,000 results from transition to the TrBL1 regime and then to the TrBL2 regime near a Reynolds number of 475,000. The behaviour of the drag coefficients is changed considerably in turbulent flow (Fig. 11d). A gradual drop in C_D is observed from a Reynolds number of 50,000 to 350,000. Similar to the PE model, Model 6-*Bare/Paint* exhibits a drop in drag at a Reynolds number of approximately 350,000 in smooth flow as the boundary layer on the model transitions to TrBL1 and TrBL2 at higher Reynolds numbers (Fig. 11e). A more gradual drop in C_D is observed in the turbulent flow results in Fig. 11e compared to the results in smooth flow, consistent with the behaviour observed for the PE model.

The cable model with concentric rings was painted during the test program and was tested in smooth and turbulent flow. The force coefficients for Model 7-*Rings/Paint* are shown in Fig. 11f. The drag coefficient exhibits a plateau in C_D over an extended range of Reynolds numbers in smooth flow. The presence of the rings appear to maintain the TrBL0 regime over a wider range of Reynolds numbers. The presence of the plateau in C_D and the minimum drag coefficient at $\varphi = 90°$ (cross-flow) are similar to results reported in Kleissl and Georgakis (2012a) for an HDPE model with concentric rings. The drag coefficient at the maximum Reynolds number varies between 0.35 and 0.6. In turbulent flow, the plateau in C_D that was a characteristic in smooth flow is no longer present, and the drag coefficient exhibits a gradual drop.

Model 8-*JRSS13b-HF/Paint* was based on a scan of a stay cable with deformations that had been scaled up such that eccentricities on the order of 1%D were present. For the turbulence comparison, the model's axial rotation angle was adjusted each time the cable was yawed, such that the same stagnation point is used for each cable-wind angle. The behaviour of Model 8 in smooth and turbulent flow is compared in Fig. 11g. Turbulence has a similar effect as on other models, where a gradual drop in C_D is observed.

The results for Model 9-*Fillet/SLS* in smooth and turbulent flow are presented in Fig. 11h. The helical fillet results in a more gradual drop in C_D compared to the bare SLS model (Fig. 11a), but the drag coefficient at high Reynolds numbers is approximately 0.8 for all cable-wind angles. The results in cross-flow ($\varphi = 90°$) compare well with data presented by Kleissl and Georgakis (2012a) for an HDPE model over the range of Reynolds numbers from 50,000 to 300,000, in spite of the difference in surface roughness between the two models, indicating that the height of the fillet may play an important role in the drag characteristics of this model. The drag coefficient in smooth flow at $\varphi = 60°$ and at $\varphi = 75°$ agrees with data from Kleissl and Georgakis (2012a) up to a Reynolds number of 250,000, after which the C_D in the current study begins to increase in the supercritical Reynolds number regime. In turbulent flow, transition occurs earlier and there is generally a more gradual drop in C_D compared to the results in smooth flow.

7.4. Effect of surface roughness

A secondary objective of this study was to evaluate the effect of surface roughness on measured force coefficients and to establish if models fabricated with SLS are representative of the aerodynamic behaviour of an HDPE stay cable sleeve. The force coefficients of three bare, cylindrical models are compared in smooth flow in Fig. 12a. The Model 1-*Bare/SLS* is approximately 6 times rougher than the Model 6-*Bare/Paint* and Model 5-*Bare/PE*. As a result of this added roughness, Model 1 experiences transition at a lower Reynolds number than the other two models, a higher minimum drag coefficient, and a higher drag at the maximum wind speeds. In addition to having an earlier onset of transition, Model 1-*Bare/SLS* exhibits smaller variations in lift compared to the smoother models. A higher surface roughness will cause the TrBL1 regime to exist for only a short range of Reynolds numbers before moving
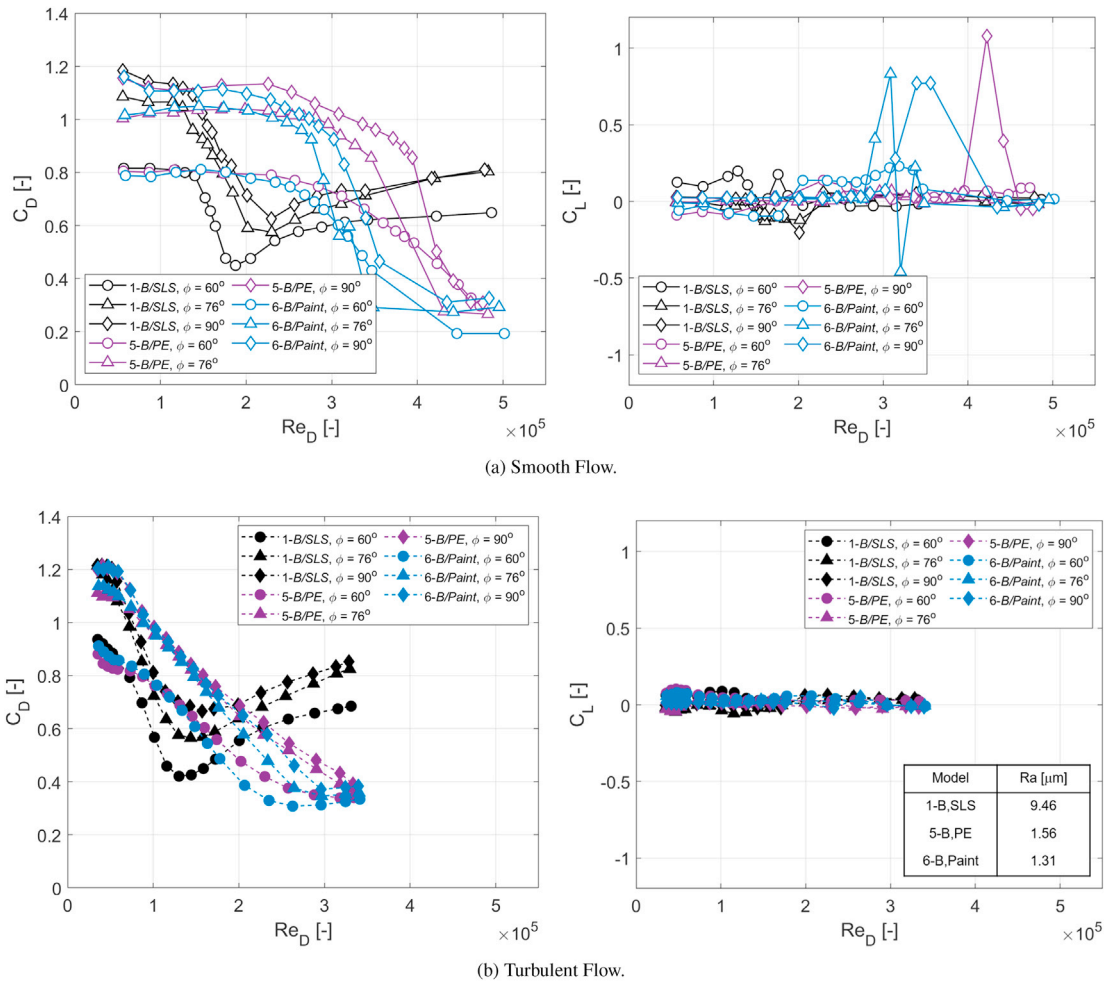
(a) Smooth Flow.

(b) Turbulent Flow.

Fig. 12. Effect of surface roughness on force coefficients for bare cable models.

to the TrBL2 regime, which is associated with symmetric separation bubbles on each side of the cable and a near-zero lift coefficient. The machined PE cylinder used in the current experiment has similar surface roughness characteristics as an HDPE stay cable section. Model 6-*Bare/Paint* had been used previously in 2015 by Christiansen et al. (2017) and was used in the current study to establish the similarities or differences between a PE model and a painted SLS model. The painted (Model 6) and PE (Model 5) models both exhibit typical transition behaviour for a smooth cylinder, but the painted SLS model experiences the onset of boundary layer transition at a lower Reynolds number than the PE model. The mean roughness values for the painted model are lower than those for the PE model, and so it may have been anticipated that the painted model would have undergone transition at a higher Reynolds number. However, the painted SLS model (Model 6) had surface scratches, some glue residue from a previous installation/removal of a helical fillet, and other surface imperfections that aren't reflected in the point measurements that were used to quantify the model roughness. In contrast, the machined PE model had a uniform surface finish which resulted in the later transition of the model. In turbulent flow (Fig. 12b), the behaviour of the raw SLS model (Model 1) is also different from the other two models and would lead to an overprediction of C_D at high Reynolds numbers. The painted and PE models experience similar behaviour throughout the range of Reynolds numbers that were tested, with a gradual drop in C_D and a C_L near zero for most of the examined Reynolds-number range. These results therefore provide confidence that the fabrication of models with SLS and paint provides an adequate representation of the aerodynamic behaviour of an HDPE cable.

For each of the bare cable models shown in Fig. 12a, variations in

mean lift are observed in smooth flow over the range of Reynolds numbers where the drag coefficient is dropping, corresponding to the transition from the TrBL0 boundary layer regime to the asymmetric TRBL1 regime. The large increase in C_L in cross-flow (flow perpendicular to the main axis of the cable) for Models 5 and 6 is attributed to the formation of a single low pressure lobe on one side of the model in the TrBL1 regime. This behaviour was repeated in a separate speed sweep (not shown) and has also been observed in Kleissl and Georgakis (2012a) on an HDPE stay cable model. The effect of turbulence was to attenuate the large fluctuations in lift that had been observed on the bare models (12b). This resulted in a C_L near zero throughout the Reynolds number range in turbulent flow. At certain conditions, the lift coefficient is observed to change its sign with an increase in Reynolds number in Fig. 12b. This is hypothesized to be associated with small differences in the boundary layer behaviour (and the associated suction peak and separation characteristics) on either side of the cable.

Although the characteristics of the bare models used in the current experiment differ somewhat from models used in other studies, a number of the general outcomes of the roughness study with the bare cable models can be compared to results available in literature for cables in cross-flow ($\varphi = 90°$). Results by Benidir et al. (2015) measured surface pressures and evaluated the transition behaviour of several HDPE cable models with an eccentricity on the order of 1%D. The roughness values of the cables in the study reported by Benidir et al. (2015) were 1.29–1.43 μm for a 250 mm diameter cable model, and were similar to the roughness of the bare painted and PE models used in the current study. Benidir et al. (2015) had observed the onset of transition (from TrBL0 to TrBL1 regimes) at Reynolds numbers on the order of 2.63×10^5 to 2.98×10^5

for a 200 mm diameter cable model, depending on the axial rotation angle of the model. In the current study, the onset of transition for Model 6-*Bare/Paint* occurred at a Reynolds number approaching 3×10^5. The Reynolds number at which the painted SLS model undergoes transition also agrees well with other results in literature (Kleissl and Georgakis, 2012b).

A study by Matteoni and Georgakis (2012) presented the effects of model circularity and turbulence on HDPE cable models with a mean roughness value on the order of 0.7–1 µm. The onset of the critical Reynolds number regime was dependent on the axial rotation angle of the model and the upper limit of the critical Reynolds number regime was on the order of 3×10^5 to 3.22×10^5 with a turbulence intensity of 0.5% (Matteoni and Georgakis, 2012). The upper limit of the critical Reynolds number regime for Model 6-*Bare/Paint* in the current study is higher than what had been observed by Matteoni and Georgakis (2012) and occurred at a Reynolds number above 3.5×10^5. Although the precise limits on the critical Reynolds number regime for cables at $\varphi = 90°$ vary between studies available in literature, the current work exhibits a reasonable level of agreement with other data given the differences in the experimental setups and cable models.

The levels of turbulence in the current experiment and that of Matteoni and Georgakis (2012) were different, but nevertheless some general observations about the effect of turbulence on the aerodynamic behaviour of models in cross-flow can be discussed. The gradual drop in drag coefficient observed for Model 6-*Bare/Paint* in turbulent flow (I_u ranges from 3.3 to 5.6%) in Fig. 12b has some similarities with results presented in Matteoni and Georgakis (2012) that had a turbulence intensity of 1.1%. In both cases, transition in the boundary layer begins earlier and is more gradual compared to results in smooth flow. A C_D of 0.8 is observed near a Reynolds number of 2×10^5 and a C_D of 0.4 is observed near a Reynolds number of 3×10^5 in Matteoni and Georgakis (2012), with some variation due to the axial rotation angle of the model, and these values are similar to what had been observed in Fig. 12b. Matteoni and Georgakis (2012) had observed a reduction in the mean lift coefficients when the turbulence intensity was increased from 0.5% to 1.1%. In the current work, at higher levels of turbulence than those used by Matteoni and Georgakis (2012), the lift coefficient is seen to be near zero throughout the Reynolds number range that was evaluated, suggesting that elevated levels of turbulence intensity can result in further suppression of the mean lift coefficient for bare models.

The study by Hojo et al. (2000) evaluated the drag coefficient behaviour of models with varying levels of surface roughness. The results presented by Hojo et al. (2000) for a model at $\varphi = 90°$ indicated that an order-of-magnitude increase in roughness from 3 µm to 30 µm caused the onset of the critical Reynolds number regime to decrease from approximately 2.2×10^5 to approximately 1×10^5. This general behaviour is

consistent with the change in drag coefficient characteristics observed by comparing Model 1-*Bare/SLS* to Model 6-*Bare/Paint* in Fig. 12a. Model 1-*Bare/SLS* had a mean roughness parameter that was approximately 6 times greater than Model 6-*Bare/Paint*, and the onset of the critical Reynolds number regime decreases by a similar amount to what had been observed in the study by Hojo et al. (2000), in which the roughness had been increased by a factor of 10.

The study of roughness effects also included the model with concentric rings, which was tested with an as-printed SLS finish (Model 2) and after the same physical model had been painted (Model 7). The mean roughness value for the Model 7-*Rings/Paint* was $R_a = 1.07$ µm. The mean roughness of the equivalent model with an SLS finish (Model 2) was not measured, but was similar to (same printer, same surface finish) the bare SLS cable (Model 1) described above ($R_a = 9.46$ µm). The force coefficients of the two models with rings are compared in smooth flow in Fig. 13. Despite the presence of rings, the surface roughness still drove the smooth-flow drag coefficient behaviour. The ring geometry covers less of the span than patterns such as the helical strakes or the dimples, and therefore it is hypothesized that the surface roughness in the regions between the rings played a role in the development of the aerodynamic phenomena. The addition of paint on Model 7 delays the onset of the transition from TrBL0 to TrBL1 by a Reynolds number of approximately 1×10^5. The painted model also has lower drag coefficient results at high wind speeds. The lift coefficient results in Fig. 13 demonstrate that the models with rings exhibit effectively no variations in mean lift over the full range of Reynolds numbers. The presence of the rings may limit the magnitude of the axial flow component along the cable, compared to a bare cable. Based on the results in Figs. 12 and 13, models that are fabricated with the SLS rapid-prototyping technique and, that are sanded and painted, replicate with more fidelity the surface characteristics of the PE.

7.5. Comparison of surface geometry

The primary objective of the current study was to compare the effect of surface geometry on models with a controlled, consistent cross-section. The force coefficients for the models with a bare surface, rings, helical strakes, dimples, and a helical fillet are compared in Fig. 14. All of the models shown in Fig. 14 have an SLS surface finish and a circular cross-section. Additionally, the cross-sectional shape of the helical fillet, helical strake, and ring geometry is rectangular and consistent between the models (1.04%D wide × 3.12%D high).

In smooth and turbulent flow, it was observed that the cable Model 3-*Strakes/SLS* has similar drag coefficient characteristics at the maximum Reynolds number as the model with dimples, but with a more gradual change in C_D over the full range of Reynolds numbers. The helical strake
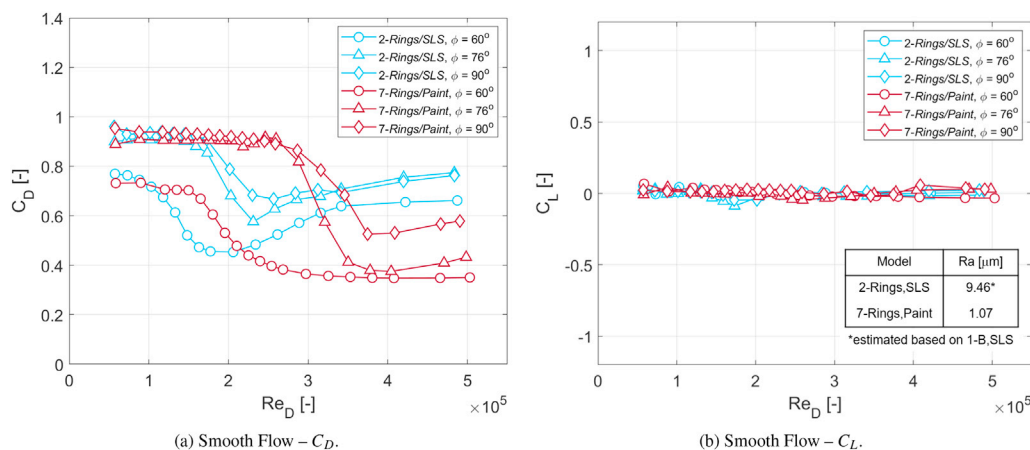

(a) Smooth Flow – C_D.　　　　　　　　　　　　(b) Smooth Flow – C_L.

Fig. 13. Effect of surface roughness on force coefficients for cable models with rings (Models 2 and 7). Smooth flow.

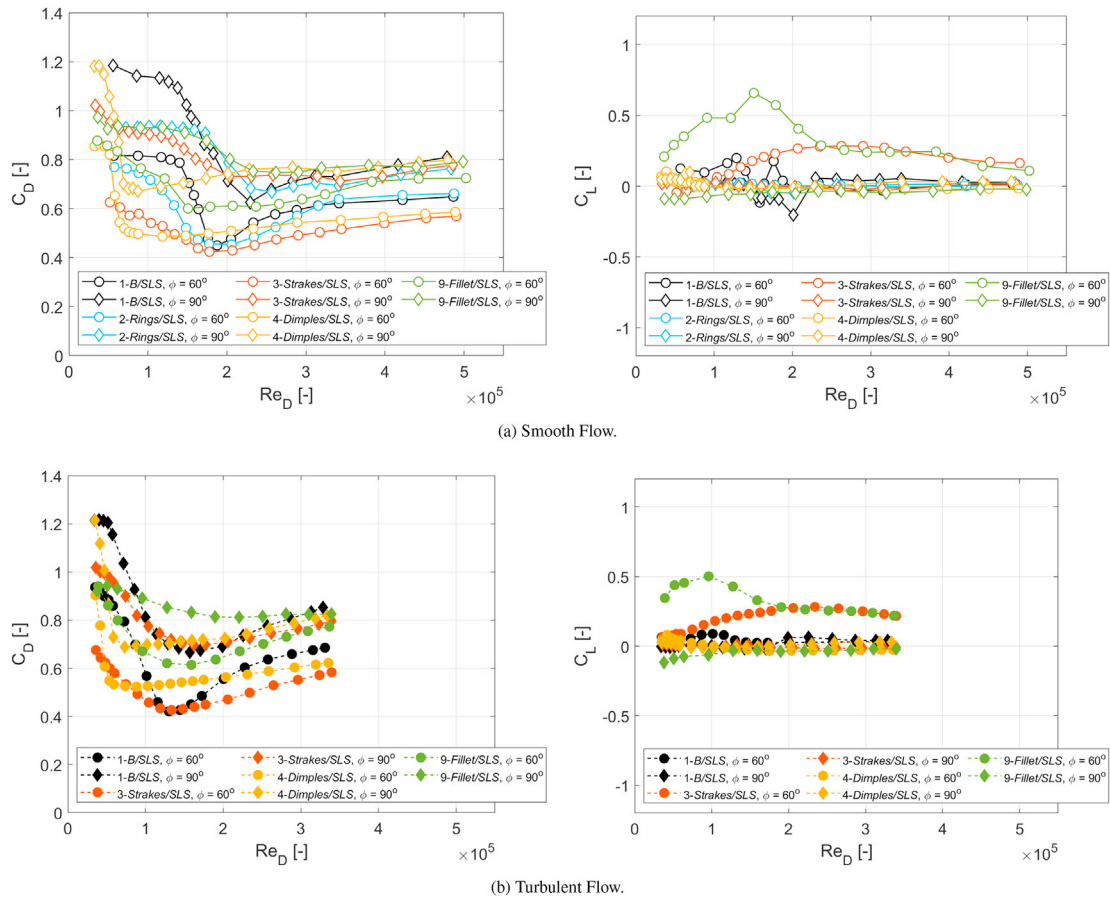(a) Smooth Flow.

(b) Turbulent Flow.

Fig. 14. Effect of surface geometry for models with an SLS finish.

geometry exhibited the lowest C_D at the maximum Reynolds number in both smooth and turbulent flow. Because of the helical pattern of Models 3-*Strakes/SLS* and 9-*Fillet/SLS*, the orientation of the pattern with respect to the wind will be different on the port and starboard sides of the cable. As a result, both models generate lift at various cable wind angles. Interestingly, the direction of lift for Model 3-*Strakes/SLS* was observed to change at low and high Reynolds numbers for cable-wind angles of $\varphi = 60°$, $75.5°$, and $104.5°$. For the case at $\varphi = 60°$, the lift force was small at low Reynolds number and within the accuracy of the measurement of the balance but the trend was similar to the other cable-wind angle cases

which had larger lift forces measured. In turbulent flow, the plateaus in drag that had been observed in smooth flow after the TrBL2 regime for Models 3 and 9 are no longer present, and the drag coefficient begins increasing at an earlier Reynolds number. The peak lift coefficient shifts to a lower Reynolds number in turbulent flow, but the overall magnitude of the lift coefficient is similar in both types of flow. The lift coefficient generated by the helical strake and helical fillet models has a similar magnitude above a Reynolds number of 2×10^5 and is due to the difference in the orientation of the surface geometry pattern on the port and starboard sides of the cable.
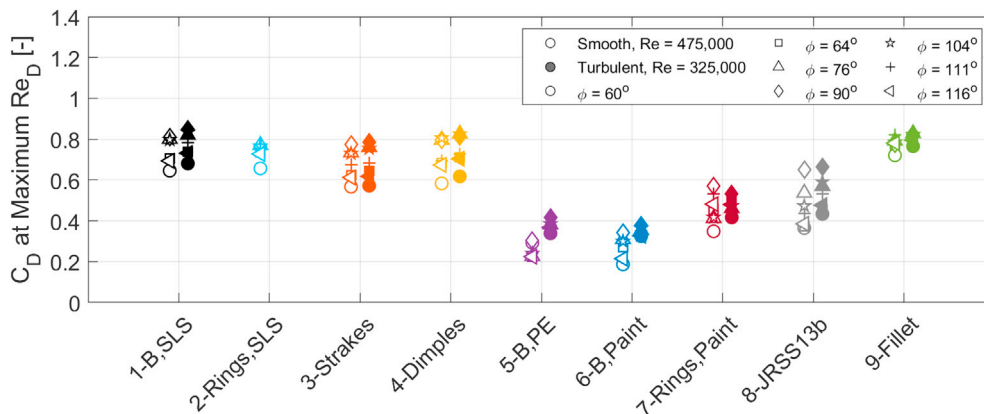

Fig. 15. Comparison of the drag coefficient of all models at the maximum Reynolds number. Test data have been interpolated to a maximum Reynolds number of 475,000 in smooth flow and to a maximum Reynolds number of 325,000 in turbulent flow.

The lift coefficient for Models 2-*Rings/SLS* and 4-*Dimples/SLS* is near-zero in smooth flow. In turbulent flow, Models 2-*Rings/SLS*, 4-*Dimples/SLS*, all three bare models, and 7-*Rings/Paint* (not shown) have a C_L near zero throughout the range of Reynolds numbers that were tested. The model with rings (Model 2) and the bare SLS model (Model 1) have similar behaviour in drag following initial transition.

In cross-flow ($\varphi = 90^o$), all five models presented in Fig. 14a have a similar C_D of between 0.75 and 0.8 at the maximum Reynolds number. The convergence of the C_D values for four of the models is observed as well in turbulent flow in Fig. 14b. Note that the Model 2-*Rings/SLS* was not tested in turbulent flow.

The effect of turbulence is similar on all models. The initial transition from TrBL0 to TrBL1 is pushed to a lower Reynolds number and the rise in drag associated with the supercritical flow regime begins at a lower Reynolds number and increases at a higher rate, compared to the results in smooth flow.

Even though the models with different surface geometries in Fig. 14 have an as-printed SLS surface finish, the resulting drag coefficients are not significantly different from values reported in literature for similar geometries. This implies that the surface geometry patterns and their height (relative dimension with respect to the cable diameter) are having a more dominant effect on the flow development compared to the surface texture. The trends observed in Fig. 14 for cables with an as-printed SLS surface finish have many similarities with published work by Kleissl and Georgakis (2012a) and Kleissl and Georgakis (2012b) and are considered to be representative of tests using full-scale HDPE sections.

The drag coefficients at the maximum Reynolds number for all of the cable models from the smooth flow and turbulent flow tests are compared in Fig. 15. The drag coefficients in smooth flow were interpolated to a Reynolds number of 4.75×10^5 and those in turbulent flow were interpolated to a Reynolds number of 3.25×10^5. These Reynolds numbers correspond to wind speeds of 36 and 25 m/s in smooth and turbulent flow, respectively, for a 0.2 m diameter stay cable. The results in Fig. 15 provide a means to compare the range of drag coefficients observed for each model at high wind speeds and confirms several of the observations noted above. Of the models with surface geometry features and an SLS surface finish, Model 3-*Strakes/SLS* has the lowest range of drag coefficients, which are also similar to those from Model 4-*Dimples/SLS*. Fig. 15 also demonstrates that the Model 5-*Bare/PE* and Model 6-*Bare/Paint* have similar drag coefficients at high Reynolds numbers.

8. Conclusions

This manuscript has documented the results of a wind-tunnel evaluation of the aerodynamic behaviour of stay cables in dry conditions. The objectives of the study were to evaluate the aerodynamic forces for static stay cable models with a bare surface and with different cable surface geometries (rings, helical strakes, helical fillet, pattern-indented surface) in smooth and turbulent flow. Future work with the same data set will investigate unsteady aerodynamic phenomena associated with the various models used in the study.

The results obtained under these conditions revealed the following aerodynamic behaviour.

8.1. General

- Control of the fabrication process allowed models to be fabricated with a circular cross-section. The high degree of circularity allowed the effects of cable surface roughness and surface geometry to be evaluated independently of cable shape.
- The model results in the current study cannot be compared directly to results in literature due to the surface roughness (SLS), circular cross-section, and differences in model installation in the wind tunnel. Nevertheless, the overall trends have many similarities with published data in literature. This implies that the surface geometry (pattern and relative dimension with respect to the cable diameter)

has a more dominant effect on the flow development compared to the surface texture. The trends observed in the current study for cable models with as-printed SLS surface finish are considered to be representative of tests using full-scale HDPE sections.

8.2. Surface geometry

- On models with surface geometry (fillet, strakes, rings, dimples), the trends in drag and lift coefficient were similar to results reported in literature using HDPE models. The drag coefficients were greater in the current study by approximately 0.05, which may be due in part to the surface roughness of the SLS models.
- The helical fillet and helical strake models have a different pattern orientation to the flow on the port and starboard sides of the cable and produce lift in smooth and turbulent flow. The lift coefficient in the helical strake and helical fillet models has a similar magnitude above a Reynolds number of 200,000.
- Of all of the geometries that were evaluated, the helical strake geometry exhibited the lowest C_D at the maximum Reynolds number in both smooth and turbulent flow. The helical strakes have similar drag coefficient characteristics at the maximum Reynolds number as the model with dimples, but with a more gradual change in C_D over the full range of Reynolds numbers.
- In cross-flow ($\varphi = 90^o$), i.e. when the flow is perpendicular to the main axis of the cable, all the models with surface geometry features have a similar C_D of between 0.75 and 0.8 at the maximum Reynolds number in smooth flow. The convergence of the C_D values for the models in cross-flow was observed as well in turbulent flow.

8.3. Surface roughness

- The surface roughness of the bare cable models played a significant role in the boundary layer transition and in the behaviour of the drag coefficient. The surface roughness of the bare SLS model was 6 times higher than the surface roughness of the painted SLS model and the PE model. Boundary layer transition occurred earlier for the rough model and the drag coefficient at high speeds was three times greater than the painted and PE models in smooth flow.
- Cable models made in SLS with paint had a similar surface roughness than the cable model made in PE. The painted SLS models exhibited similar drag and lift behaviour as results for the PE model in the current study and for HDPE models reported in literature.

8.4. Turbulence

- The effect of turbulence on the aerodynamic response of all of the cable models was similar. Turbulence promoted early transition from the TrBL0 to TrBL1 boundary layer regimes, caused the minimum drag coefficient to occur at a Reynolds number that was 0.5×10^5 to 1×10^5 lower than for smooth flow, and saw the rise in drag associated with the supercritical regime (TrBL3) occur at an earlier Reynolds number than smooth flow. The presence of turbulent flow resulted in a more gradual decrease in drag for all of the cable models and eliminated variations in mean lift for all symmetric models.

Declaration of competing interest

The authors declare that they have no known competing financial interests or personal relationships that could have appeared to influence the work reported in this paper.

Acknowledgements

References

Benidir, A., Flamand, O., Dimitriadis, G., 2018. The impact of circularity defects on bridge stay cable dry galloping stability. J. Wind Eng. Ind. Aerod. 181, 14–26.

Benidir, A., Flamand, O., Gaillet, L., Dimitriadis, G., 2015. Impact of roughness and circular-defect on bridge cables stability. J. Wind Eng. Ind. Aerod. 137, 1–13.

Bosch, H., Pagenkopf, J., 2017. Development of a robot to measure stay cable roundness. In: Proc. Of the International Symposium on the Dynamics and Aerodynamics of Cables. Porto, Portugal.

Burlina, C., Georgakis, C., Larsen, S., Egger, P., 2016a. Comparative analysis of bridge cables with concave fillets. In: Proc. Of the First International Symposium on Flutter and its Application.

Burlina, C., Georgakis, C., Larsen, S., Egger, P., 2016b. Optimization of bridge cables with concave fillets. In: Proc. Of the 8th International Colloquium on Bluff Body Aerodynamics and Applications. Boston, Massachusetts, USA.

Cheng, S., Larose, G., Savage, M., Tanaka, H., Irwin, P., 2008. Experimental study on the wind-induced vibration of a dry inclined cable - part I: Phenomena. J. Wind Eng. Ind. Aerod. 96, 2231–2253.

Christiansen, H., Larose, G., Jakobsen, J., Bosch, H., 2017. Effects of cross-sectional shape distortions on bridge stay cable aerodynamics. In: Proc. Of the International Symposium on the Dynamics and Aerodynamics of Cables (ISDAC 2017), pp. 167–175.

D'Auteuil, A., 2010. Manipulation of the boundary layer transition to enhance the aerodynamic performance of athletes. PhD thesis.

D'Auteuil, A., McTavish, S., Raeesi, A., 2019. A new large-scale dynamic rig to evaluate rain-wind induced vibrations on stay cables: design and commissioning. In: Proc. Of the 15th International Conference on Wind Engineering. Beijing, China.

Demartino, C., Koss, H., Georgakis, C., Ricciardelli, F., 2015. Effects of ice accretion on the aerodynamics of bridge cables. J. Wind Eng. Ind. Aerod. 138, 98–119.

Hojo, T., 2015. Control of flow around a circular cylinder using a patterned surface. In: WIT Transactions on Modelling and Simulation, vol. 59.

Hojo, T., Okada, H., Yamazaki, S., 2000. Development of lowdrag aerodynamically stable cable with indented processing. Tech. Rep. Report No. 82. Nippon Steel.

Katsuchi, H., Yamada, H., Sakaki, I., Okado, W., 2017. Wind-tunnel investigation of the aerodynamic performance of surface-modification cables. Engineering 3, 817–822.

Kleissl, K., Georgakis, C., 2012a. Comparison of several innovative bridge cable surface modifications. In: Proc. Of the Seventh International Colloquium on Bluff Body Aerodynamics and Applications (BBAA7). Shanghai, China.

Kleissl, K., Georgakis, C., 2012b. Comparison of the aerodynamics of bridge cables with helical fillets and a pattern-indented surface. J. Wind Eng. Ind. Aerod. 104–106, 166–175.

Kumarasena, S., Jones, N., Irwin, P., Taylor, P., 2007. Wind-induced vibration of stay cables. Tech. Rep. FHWA-HRT-05-083. US Federal Highway Administration.

Larose, G., Savage, M., Jakobsen, J., 2003. Wind tunnel experiments on an inclined and yawed circular cylinder in the critical Reynolds number range. In: Proc. Of the 11th International Conference on Wind Engineering, pp. 1705–1712.

Larose, G.L., D'Auteuil, A., 2014. Wind tunnel investigations of an inclined stay cable with a helical fillet. Tech. Rep. FHWA-HRT-14-070. Federal Highway Administration.

Matteoni, G., Georgakis, C., 2012. Effects of bridge cable surface roughness and cross-sectional distortion on aerodynamic force coefficients. J. Wind Eng. Ind. Aerod. 104–106, 176–187.

McTavish, S., Raeesi, A., D'Auteuil, A., Yamauchi, K., Sato, H., 2018. An investigation of the mechanisms causing large-amplitude wind-induced vibrations in stay cables using unsteady surface pressure measurements. J. Wind Eng. Ind. Aerod. 183, 19–34.

Miyata, T., Fujiwara, T., Yamada, H., 1998. Wind-resistant design of cables for the tatara bridge. Tech. Rep. 79. ETH Zurich.

Yamauchi, K., Uejima, H., McTavish, S., Larose, G., 2016. Effects of a helical fillet on the wind-induced response of bridge cables in dry conditions. Proc. Of the 8th International Colloquium on Bluff Body Aerodynamics and Applications.

Zdravkovich, M.M., 1997. Flow Around Circular Cylinders, vol. 1. Oxford University Press, Oxford, UK.